

Nonspecular electron transmission leads to drastically reduced contact resistance between dissimilar semiconductors

Qichen Song,^{1,*} Jiawei Zhou,^{1,2} and Gang Chen^{1,†}

¹*Department of Mechanical Engineering, Massachusetts Institute of Technology, Cambridge, Massachusetts 02139*

²*Department of Materials Science and Engineering, Stanford University, Stanford, California 94305*

The contact resistance between two dissimilar semiconductors is determined by the carrier transmission through their interface. Despite the ubiquitous presence of interfaces, quantitative simulation of charge transport across such interfaces is difficult, limiting the understanding of interfacial charge transport. This work employs Green's functions to study the charge transport across representative Si/Ge interfaces. For perfect interfaces, it is found that the transmittance is small and as a consequence the contact resistance is high not only because the mismatch of carrier pockets makes it hard to meet the momentum conservation requirement but also because the incompatible symmetries of the Bloch wavefunctions of the two sides. In contrast, atomic mixing at the interface increases the carrier transmittance as the interface roughness opens many nonspecular transmission channels, which greatly reduce the contact resistance compared with the perfect interface. Specifically, we show that disordered interfaces with certain symmetries create more nonspecular transmission. The insights from our study will benefit the future design of high-performances heterostructures with low contact resistance.

I. INTRODUCTION

The importance of interfaces in advanced semiconductor devices has been clearly pointed out by Herbert Kroemer with his famous statement, “the interface is the device”[1]. Semiconductor heterostructures play essential roles in vertical-cavity surface-emitting lasers[2–4], heterostructure bipolar transistors[5, 6], quantum cascade lasers[7], quantum well infrared photodetectors[8], thermionic microcoolers[9, 10], bipolar transistors[11], spin qubit devices[12, 13], thermoelectric power generators[14–17], *etc.* However, the interfaces in heterostructures strongly scatter electrons and cause the contact resistance[18–21]. The interface scattering probabilities are not only determined by the intrinsic properties of bulk materials, but by the non-intrinsic properties such as the interface structures. Specifically, the interface roughness due to atomic mixing[22], as a common type of interface disorder, alters the contact resistance. In order to design proper interface structures that minimize interfacial resistance, it is crucial to understand how the atomic mixing affects electron scattering at interfaces.

The nonequilibrium Green's function (NEGF) is often used to describe the structure-dependent charge transport[23]. Many works using NEGF combined with Landauer formula for conductance are conducted to study the transport across molecular junctions[24–27], nanotransistors[28, 29], grain boundaries in two-dimensional materials[30], metal-semiconductor interfaces[31, 32], metal-metal interfaces in magnetic multilayers [33–36] and semiconductor interfaces[37, 38]. In particular, Bellotti *et al.* investigated the carrier transport through semiconductor interfaces in the presence of positional and compositional disorders using NEGF and found that the disorder significantly impeded the coherent propagation of carriers through mul-

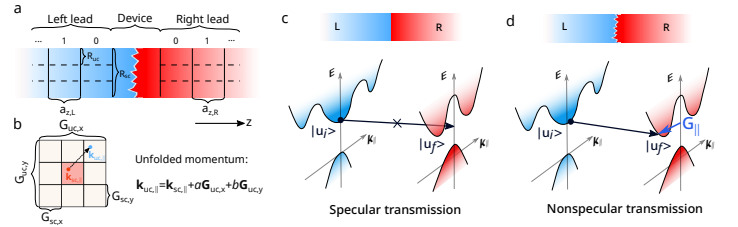


Figure 1. (a) The partitioning for Green's function calculation with repeated unitcell in the lead region being numbered with 0, 1 (b) The transverse momentum conservation law and how the transverse momenta in the unitcell representation and the supercell representation are related. (c) Specular transmission process through a perfect interface where the transverse momentum is conserved, $\mathbf{k}_{i,\parallel} = \mathbf{k}_{f,\parallel}$. (d) Nonspecular transmission processes through a disordered interface, where $\mathbf{k}_{i,\parallel} = \mathbf{k}_{f,\parallel} + m\mathbf{G}_x + n\mathbf{G}_y$, allows the scattering between valleys with different \mathbf{k}_{\parallel} .

iple interfaces[37]. Tibaldi *et al.* performed a large-scale NEGF calculation of the carrier transport in a realistic tunnel junctions for vertical-cavity surface-emitting lasers and achieved a good agreement with experimental $I - V$ curve. However, the interface roughness in the transverse directions is neglected in these works, as the computational cost of NEGF increases dramatically with the cross-section areas of the interface. Besides NEGF calculation, Daryoosh *et al.* used a simple effective mass model to study the carrier transport through barriers in metal-based superlattices and found that the nonspecular (diffuse) scattering can greatly boost the thermoelectric figure of merit zT [17]. Los studied how the transmission probability varies with the average fluctuations of potential energies due to interface disorders under the effective mass approximation[39]. However, the effective mass approximation adopted in these works can poorly describe practical semiconductors with band pockets not at zone center. Due to the multi-valley nature[15] of the band structures of semiconductors, new physics shall emerge for electron interfacial transport.

In this work, we apply the mode-resolved Green's function

* qcsong@mit.edu

† gchen2@mit.edu

formalism with tight-binding Hamiltonian to study charge transport across perfect and rough interfaces due to atomic mixing. In particular, we take advantage of the transverse translational symmetry to reduce the computational cost of surface Green's function. The tight-binding Hamiltonian makes sure the multiple carrier pockets in the Brillouin zone are properly described. We vary the degree of disorders in transverse directions and perpendicular directions and study the specular and nonspecular interface scattering processes with mode resolution. Moreover, we unveil the roles of disorders and symmetries in assisting nonspecular transmission. We show that over one order of magnitude of reduction of the specific contact resistance can be enabled by the interfacial atomic mixing.

II. METHODOLOGY

In the Green's function calculation, we first divide the system into three regions, two semi-infinite lead regions and a device region, as depicted in Fig. 1 (a). The repeated cells along z direction in the lead region are indexed by $0, 1, \dots$ and the period length is $a_{z,\alpha}$ with $\alpha = x, y$. The whole supercell structure is periodic parallel to the interface. Inside the lead region, there are $N_{uc,x} \times N_{uc,y}$ identical unitcells along the transverse directions. The transverse lattice vector for the supercell is $\mathbf{R}_{sc,\alpha} = N_{uc,\beta} \mathbf{R}_{uc,\beta}$ with $\beta = x, y$, where $\mathbf{R}_{uc,\beta}$ is the transverse lattice vector for the unitcell. As a result, the transverse momentum in the supercell representation can be uniquely unfolded in a momentum defined in the unitcell representation, as elucidated in Fig. 1 (b). The unfolded momentum can be expressed by,

$$\mathbf{k}_{uc,\parallel} = \mathbf{k}_{sc,\parallel} + a\mathbf{G}_{sc,x} + b\mathbf{G}_{sc,y} \quad (1)$$

where a and b are integers to be determined. Finding the correct pair of a and b is known as an unfolding problem and we use the unfolding scheme by Popescu and Zunger[40] to resolve the correct $\mathbf{k}_{uc,\parallel}$.

We consider the elastic interface scattering limit, where the energy E of the incident electron is conserved. In addition, the in-plane translational symmetry of the supercell dictates that the transverse momentum $\mathbf{k}_{sc,\parallel}$ must be conserved during an interface scattering event. When the device region contains a perfect interface with the same in-plane periodicity as the lead region, the transverse momentum $\mathbf{k}_{uc,\parallel}$ is also conserved. However, when the device region consists of a rough interface, $\mathbf{k}_{uc,\parallel}$ is not always conserved. This is because the interface roughness breaks the internal transverse translational symmetry within the supercell and $\mathbf{k}_{sc,\parallel}$ can be unfolded into different $\mathbf{k}_{uc,\parallel}$ for the incident state and the transmitted state. As shown in Fig. 1 (c), for a perfect interface, $\mathbf{k}_{uc,\parallel}$ is conserved, and we denote this type of scattering process the specular transmission. For a rough interface shown in Fig. 1 (d), $\mathbf{k}_{uc,\parallel}$ can be either conserved or nonconserved. Particularly, we denote the scattering process with nonconserved $\mathbf{k}_{uc,\parallel}$ the nonspecular transmission.

We define the transmission probability matrix from the left side $T_{ji}(E, \mathbf{k}_{sc,\parallel})$ as the ratio between the normal current of the transmitted state j to the incident state i . For-

mally, we can express the specular and nonspecular transmission probability matrix by,

$$\begin{cases} T_{s,ji}(E, \mathbf{k}_{sc,\parallel}) = T_{ji}(E, \mathbf{k}_{sc,\parallel}), & \text{when } \mathbf{k}_{uc,\parallel,j} = \mathbf{k}_{uc,\parallel,i} \\ T_{ns,ji}(E, \mathbf{k}_{sc,\parallel}) = T_{ji}(E, \mathbf{k}_{sc,\parallel}), & \text{when } \mathbf{k}_{uc,\parallel,j} \neq \mathbf{k}_{uc,\parallel,i} \end{cases} \quad (2)$$

The elements of the transmission probability matrix from the left side is given by,

$$T_{ji}(E, \mathbf{k}_{sc,\parallel}) = |t_{RL,ji}(E, \mathbf{k}_{sc,\parallel})|^2 \quad (3)$$

where the transmission matrix $t_{RL,ji}(E, \mathbf{k}_{sc,\parallel})$ is related to the Green's function[41],

$$t_{RL}(E, \mathbf{k}_{sc,\parallel}) = i\sqrt{V_R^r}[U_R^r]^{-1}G_{N+1,0}[U_L^{a\dagger}]^{-1}\sqrt{V_L^a} \quad (4)$$

The formal definitions and detailed calculations of the velocity matrices $V_{R/L}^{r/a}$, eigenvector matrices $U_{R/L}^{r/a}$ and Green's function $G_{N+1,0}$ can be found in the Appendix A. Note that the calculation of the velocity matrices and eigenvector matrices require the surface Green's function $g_{L/R}^{a/r}(E, \mathbf{k}_{sc,\parallel})$. We apply the Fourier transform to the Hamiltonian to obtain the block-diagonal surface Green's function. Then, we apply the inverse Fourier transform to obtain the surface Green's function. These procedures allow us to invert small matrix multiple times rather than directly inverting the large matrix, which greatly boost the computational efficiency. The detailed implementation can be found in our prior work on diffuse phonon scattering by rough interfaces[42].

III. BAND STRUCTURES

We study the [001] Si/Ge interface as it is a classical semiconductor interface used in a wide range of applications such as quantum information storage[13], strained field-effect transistors[43, 44] and thermoelectrics[15, 45]. To start with, we examine the bands structures for Si and Ge individually. We use $sp^3d^5s^*$ Slater-Koster tight-binding model[46, 47] to compute the band structure, with hopping integral parameterizations from Niquet *et al*[48]. More specifically, the hopping integral varies with bond lengths according to a power law,

$$V_{\alpha\beta\gamma}(L) = V_{0,\alpha\beta\gamma} \left(\frac{L}{L_0} \right)^{\chi_{\alpha\beta\gamma}} \quad (5)$$

where α and β refer to the orbital types, γ is the type of bond, L is the bond length, L_0 is equilibrium bulk bond length, $V_{0,\alpha\beta\gamma}$ is the hopping integral for unstrained bond, and $\chi_{\alpha\beta\gamma}$ is the power law exponent. The band structures using this set of hopping integrals have shown an excellent agreement with GW calculations with various strain ratios[48]. The bulk Si and Ge have mismatched lattice constants with $a_{Si} = 5.431 \text{ \AA}$ and $a_{Ge} = 5.658 \text{ \AA}$. Correspondingly, the unstrained bond lengths for Si and Ge are 2.352 \AA and 2.450 \AA , respectively. For simplicity, we study the lattice-matched interface and we assume the Si-Si and Ge-Ge bond lengths are the same, $L = 2.398 \text{ \AA}$, which is relaxed

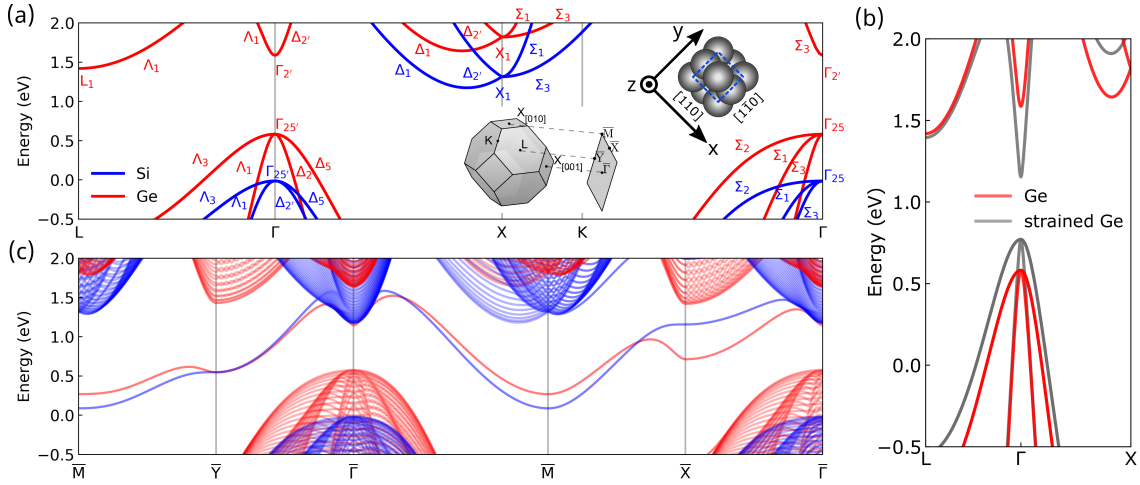


Figure 2. (a) The band structure for bulk Si, Ge along high symmetry lines in the first Brillouin zone. Left inset: the three-dimensional first Brillouin zone of Si (Ge) and its projection on the (001) plane. Right inset: the atomic structure for Si (Ge) unitcell along [001] direction. (b) The band structures for Ge and tensile-strained Ge (2%). (c) The band structures for Si and Ge slabs along high symmetry lines in the surface Brillouin zone. The slab contains 108 atom layers (27 a in thickness with a the lattice constant).

Si-Ge bond length found by Niquet *et al*[48]. Furthermore, we rescale the L_0 for Si-Si bond and Ge-Ge bond to be $L_0 = 2.398 \text{ \AA}$ to ensure that the Si's and Ge's band structures are the same with their unstrained bulk band structures[49, 50]. In our calculation, the spin-orbital coupling is not included.

First, we compare the band structures $E_n(\mathbf{k})$ of bulk Si and Ge along high-symmetry paths and examine the distributions of electron/hole pockets in the first Brillouin zone, as depicted in Fig. 2 (a), which clearly shows that the conduction band pockets for Si and Ge are distributed very differently, whereas their valence band pockets are quite similar. In particular, the highest valence bands for Si and Ge are both at Γ point. In contrast, the conduction band edge for Si is close to X point along the ΓX path (in the following, we denote this point Δ), while the conduction band edge for Ge is at L point. In addition, there are 6 pockets for Si's lowest conduction band between at Δ point, while there are 4 pockets (or 8 half-pockets) for Ge at L point. The second-lowest conduction band for Si is at X point. The second and third-lowest conduction bands for Ge is at Γ point and Δ point, respectively.

Next, we look into the symmetry properties of the Bloch wavefunctions in order to develop an understanding of how symmetry affects the transmission. In the bra-ket notation, the transmission matrix element is directly proportional to the Green's function matrix element,

$$t_{ji} \propto \langle u_j | \hat{G} | u_i \rangle \quad (6)$$

where $\hat{G} = (EI - \hat{H})^{-1}$ is the Green's function operator[51, 52]. It is easy to show that \hat{G} inherits all symmetries of \hat{H} [53]. For $|u_j\rangle$ and $|u_i\rangle$ with certain type of symmetries, the transmission matrix element t_{ji} is guaranteed to vanish according to group theory[54]. Thus, it is essential to identify the symmetries of Bloch wavefunctions of the two sides.

To describe the symmetry properties of Bloch wavefunctions in Si and Ge, the Bouckaert-Smoluchowski-Wigner

(BSW)[55] notation is adopted in Fig. 2 (a), which marks the irreducible representations for the Bloch wavefunction. The different irreducible representations of the same group (labeled by the same Greek letter with different subscripts) are orthogonal to each other. The character tables for different groups can be found in group theory textbooks[54] and online databases[56], which describes how the Bloch wavefunction transforms under certain symmetry operations. For instance, the states of the lowest conduction band of Si at Δ point transforms as Δ_1 representation under the symmetry operations of C_{4v} group. On the other hand, the states of the second-lowest conduction band in Ge at Δ point transforms as Δ_2' representation. Without the loss of generality, we consider the Δ points along the z axis [(0,0,1) axis]. In this case, one of the C_{4v} group elements is the symmetry operation $\hat{S} = \{C_4 | \tau_d\}$ with $\tau_d = \frac{1}{4}(a, a, a)$, which first rotates the Bloch wavefunction by 90 degree with respect to the z axis and then applies the translation operator by τ_d . When applying \hat{S} to a state $|u_i\rangle$ of Δ_1 symmetry, we have $\hat{S}|u_i\rangle = 1 \cdot e^{ik_z a/4} |u_i\rangle$, where k_z is the wavevector's z component. The phase factor $e^{ik_z a/4}$ appears because the space group of Si (Ge) structure is nonsymmorphic. In comparison, when applying the same operator \hat{S} to a state u_i of Δ_2' symmetry, we have $\hat{S}|u_i\rangle = -1 \cdot e^{ik_z a/4} |u_i\rangle$. Intuitively, one can regard Δ_1 as "even" and Δ_2' as "odd" in a more generalized way. The incident and transmitted states are not compatible thus they will never interact. Hence, knowing the symmetries properties of wavefunctions (*i.e.*, their irreducible representations) will be useful in the later analysis of the transmission probabilities.

Moreover, the strain effect can change the relative positions for different valleys in the reciprocal space. We find that the strain generally has a smaller impact on Si compared with Ge thus we only consider the case of applying strain to Ge. Since we have already assumed the Si and Ge have the same bond lengths $L = 2.398 \text{ \AA}$, we change the equilibrium L_0 of Ge from 2.398 \AA to 2.343 \AA while keep-

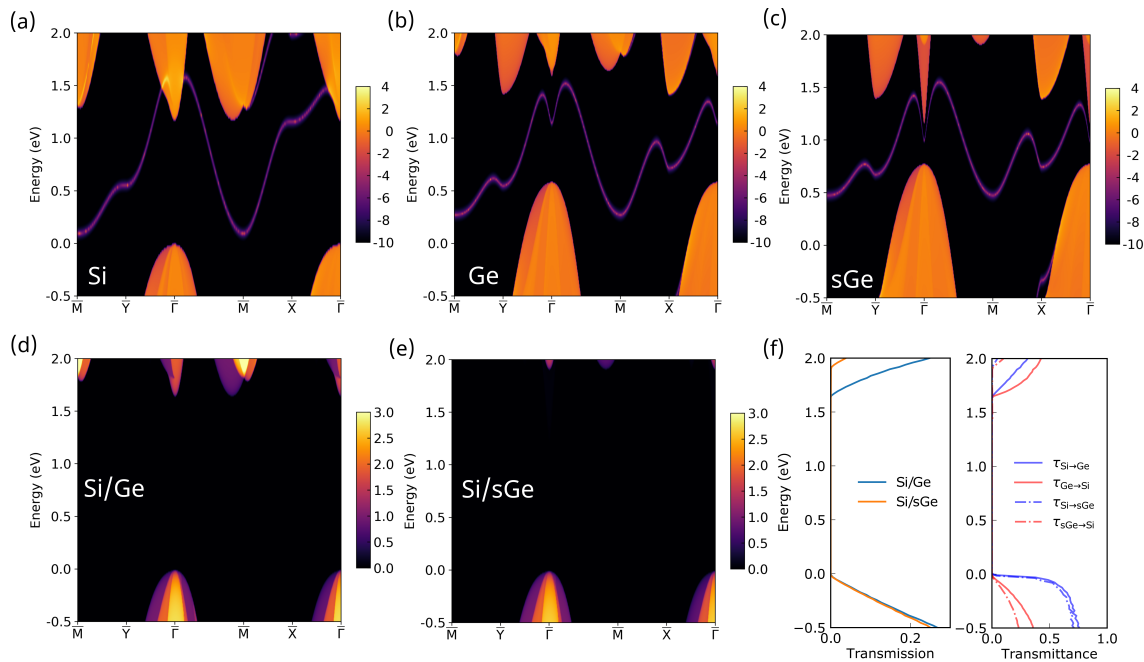


Figure 3. The surface density of states $\text{SDOS}(E, \mathbf{k}_{\text{uc},\parallel})$ for (a) Si, (b) Ge and (c) sGe. The logarithm of the surface density of state is indicated by colors and the spin degree of freedom 2 is not multiplied. The transmission spectra $T(E, \mathbf{k}_{\text{uc},\parallel})$ along high symmetry lines in the surface Brillouin zone through (d) a perfect Si/Ge [001] interface and (e) a perfect Si/sGe [001] interface. The color indicates the value of $T(E, \mathbf{k}_{\text{uc},\parallel})$. (f) Left panel: the transmission function $\Theta(E) = \frac{1}{N_{\mathbf{k}_{\text{uc},\parallel}}} \sum_{\mathbf{k}_{\text{uc},\parallel}} T(E, \mathbf{k}_{\text{uc},\parallel})$ for a perfect Si/Ge interface and a perfect Si/sGe interface ($N_{\mathbf{k}_{\text{uc},\parallel}} = 40 \times 40$ is used). Right panel: the transmittance $\tau_{\alpha}(E) = \frac{\Theta(E)}{\Theta_{\text{bulk},\alpha}(E)}$ from Si and Ge side, where $\Theta_{\text{bulk},\alpha}(E)$ is the transmission function for bulk α material.

ing L unchanged. The corresponding hopping integrals $V_{\alpha\beta\gamma}$ (defined in Eq. 5) are altered and the Ge band structure is accordingly changed. Effectively, we have applied a tensile strain of 2 % to Ge. In Fig. 2 (b), we compare the band structures of strained Ge (sGe for short) with the relaxed Ge. The stretched bond distance pushes the second-lowest conduction band downwards and make it the lowest conduction band. It also shifts the third-lowest band further upwards. Meanwhile, the strained Ge-Ge bond also makes the valence band upwards and thus causing a smaller bandgap. The features of the sGe band structure are consistent with other works[13, 57].

When forming an interface, the translational symmetry is broken along the direction normal to the interface, and the band structures are now projected to the two-dimensional surface Brillouin zone, as depicted in the left inset of Fig. 2 (c). We conduct a slab calculation to study the projected band structure. The slab is periodic along x and y directions and finite in z direction. The unitcell for Si (Ge) slab along [001] direction contains 4 atoms, as shown in the right inset of Fig. 2 (a). Note that the structure of Si (Ge) has mirror symmetries with respect to (110) and (1 $\bar{1}$ 0) planes. In Fig. 2 (c), we find that the highest valence bands of Si and Ge are both projected to the $\bar{\Gamma}$ point. Two out of the six lowest conduction band pockets of Si are projected to the $\bar{\Gamma}$ point, two pockets are projected to a point between $\bar{\Gamma}$ and \bar{X} point and the remaining two pockets are projected to a point between $\bar{\Gamma}$ and \bar{Y} point. As for Ge, two of the four lowest conduction band pockets at L points are projected to

the \bar{X} point and the remaining two are projected to the \bar{Y} point. Since we use a slab to compute the projected band structure, we observe the surface states[58] for Si and Ge within the bandgap. They each have two degenerate surface states within the x-y plane, one for the top surface, one for the bottom surface. However, in the direction normal to the interface (z direction), these surface states are localized thus do not contribute to the interfacial transport.

Lastly, we study the density of states for the projected band. The density of states for the projected band structures at the given energy E and transverse momentum $\mathbf{k}_{\text{uc},\parallel}$ is obtained by taking the imaginary part of retarded surface Green's function (given by Eq. A4) for the lead,

$$\text{SDOS}(E, \mathbf{k}_{\text{uc},\parallel}) = -\frac{1}{\pi} \text{Im} g_{\alpha}^r(E, \mathbf{k}_{\text{uc},\parallel}) \quad (7)$$

where g_{α}^r with $\alpha = \text{Si, Ge}$ is the retarded surface Green's function for α lead. From the density of states shown Fig. 3 (a), where we use color to indicate $\ln[\text{SDOS}(E, \mathbf{k}_{\text{uc},\parallel})]$, we identify the localized states within the bandgap, the continuum spectrum of propagating conduction band electrons and the resonant states within the continuum spectrum.

IV. TRANSMISSION THROUGH A PERFECT INTERFACE

We first study the electron transmission through a perfect interface. There are several relevant physical quanti-

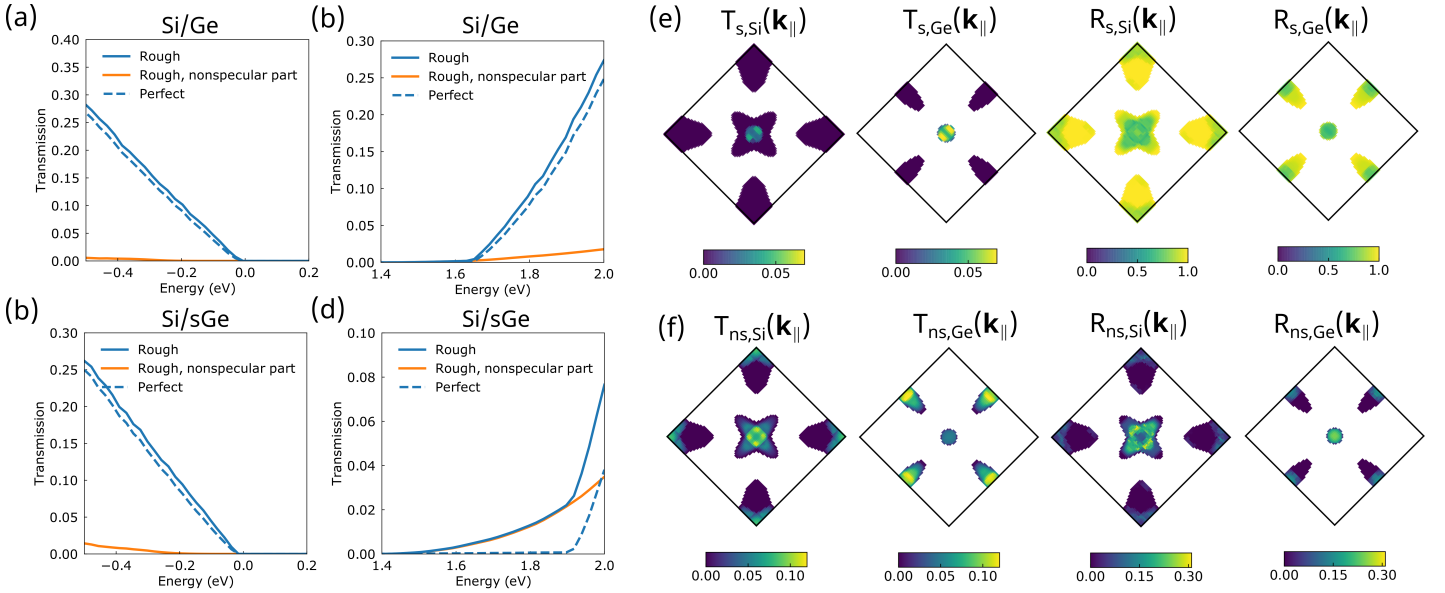


Figure 4. The ensemble-averaged total transmission function $\Theta(E)$ and nonspecular transmission function $\Theta_{\text{ns}}(E)$ through rough Si/Ge interfaces for (a) electrons and (b) holes in solid lines compared with the transmission function for a perfect interface in dashed line. 21 configurations of 2×2 , 8 ml disordered interfaces are used for ensemble average. (c) and (d): the transmission function for Si/sGe interfaces. (e) and (f): the ensemble-averaged mode-resolved specular and nonspecular scattering probabilities at $E = 1.77$ eV for rough Si/sGe interfaces defined by Eq. 8 as a function of in-plane momentum $\mathbf{k}_{\text{uc},\parallel}$. The calculation uses a 40×40 $\mathbf{k}_{\text{sc},\parallel}$ -point mesh. Effectively, it corresponds to a 80×80 $\mathbf{k}_{\text{uc},\parallel}$ mesh.

ties, and we want to clarify their physical meaning here to avoid confusion. $t_{RL,ji}(E, \mathbf{k}_{\text{sc},\parallel})$ is the transmission matrix, which is used to compute the transmission probability matrix. $T_{ji}(E, \mathbf{k}_{\text{sc},\parallel})$ is the transmission probability matrix, which described mode-to-mode transition probability, normalized by normal incident current. $T_i(E, \mathbf{k}_{\text{sc},\parallel})$ refers the transmission probability (transmittance) across the interface for an incident electron i . The transmission spectrum $T(E, \mathbf{k}_{\text{sc},\parallel})$ is the number of transmission channels including all subbands that have same E and $\mathbf{k}_{\text{sc},\parallel}$. The transmission function (we use transmission in short in figures) $\Theta(E)$ describe the total number of transmission channels at the given energy E and is the sum of all transmission channels with different $\mathbf{k}_{\text{sc},\parallel}$. Note that $t_{RL,ji}(E, \mathbf{k}_{\text{sc},\parallel})$, $T_{ji}(E, \mathbf{k}_{\text{sc},\parallel})$, $T_i(E, \mathbf{k}_{\text{sc},\parallel})$ depend on which side incident electron is from, whereas $T(E, \mathbf{k}_{\text{sc},\parallel})$, $\Theta(E)$ are independent of the side of incidence.

The transmission probability can be computed by summing the transmission probability matrix over all possible final states. And the specular part and nonspecular part of the transmission probability read,

$$\begin{cases} T_{s,i}(E, \mathbf{k}_{\text{sc},\parallel}) = \sum_j T_{s,ji}(E, \mathbf{k}_{\text{sc},\parallel}) \\ T_{\text{ns},i}(E, \mathbf{k}_{\text{sc},\parallel}) = \sum_j T_{\text{ns},ji}(E, \mathbf{k}_{\text{sc},\parallel}) \end{cases} \quad (8)$$

The transmission function is the measure of conductance channels and can be expressed by, $\Theta(E) = \Theta_s(E) + \Theta_{\text{ns}}(E)$, where the specular and nonspecular transmission function

are defined by,

$$\begin{aligned} \Theta_s(E) &= \frac{1}{N_{\mathbf{k}_{\text{sc},\parallel}}} \sum_{i, \mathbf{k}_{\text{sc},\parallel}} T_{s,i}(E, \mathbf{k}_{\text{sc},\parallel}) \\ \Theta_{\text{ns}}(E) &= \frac{1}{N_{\mathbf{k}_{\text{sc},\parallel}}} \sum_{i, \mathbf{k}_{\text{sc},\parallel}} T_{\text{ns},i}(E, \mathbf{k}_{\text{sc},\parallel}) \end{aligned} \quad (9)$$

For the case of perfect interface, all the transmission processes are specular, hence we have $T_{s,ji}(E, \mathbf{k}_{\text{sc},\parallel}) = T_{ji}(E, \mathbf{k}_{\text{sc},\parallel})$. In addition, for the perfect interface, we only need to construct a unitcell as the supercell such that the in-plane momenta in the unitcell representation and the supercell representation are the same, $\mathbf{k}_{\text{uc},\parallel} = \mathbf{k}_{\text{sc},\parallel}$.

The transmission spectrum is attained by $T(E, \mathbf{k}_{\text{uc},\parallel}) = \sum_i T_i(E, \mathbf{k}_{\text{uc},\parallel})$, where we sum over all subbands with the same E and $\mathbf{k}_{\text{uc},\parallel}$. In Fig. 3 (d) and (e), we show the transmission spectra $T(E, \mathbf{k}_{\text{uc},\parallel})$ through the Si/Ge and Si/sGe interfaces. Comparing with the surface density of states through examining the Fig. 3 (a)-(d), we see that the transmission is non-zero only when the surface density of states of Si/sGe overlap. This is due to the energy and momentum conservation requirement. For example, the Ge's lowest conduction band at \bar{X} and \bar{Y} does not have any corresponding states in Si thus cannot contribute to transmission. Most of the overlapped states are the valleys at $\bar{\Gamma}$ and along the $\bar{\Gamma}\bar{M}$ path, which corresponds to the lowest conduction band in Si, and second- and third-lowest conduction bands in Ge.

Because of the mismatch of conduction band valleys of Si and Ge, a large ‘‘transport gap’’ of 1.65 eV emerges at the $\bar{\Gamma}$ point. For a Si/sGe interface, the transmission spectra for holes change slightly from a Si/Ge interface. The transport gap is 1.91 eV, which even larger due to fewer energy and

momentum matched conduction bands. From the energy-resolved transmission and transmittance in Fig. 3 (f), we also find that strain has much smaller impact on the hole transmission than the electron transmission. This is because the valence bands stay at $\bar{\Gamma}$ point even with strain, while the strain change the position of conduction bands in reciprocal space more profoundly.

What is intriguing is that at $\bar{\Gamma}$ point, Si and sGe have overlapped conduction band pockets, yet the transmission $T(E, \mathbf{k}_{\text{uc}, \parallel})$ is still almost zero. This suggests that there are other factors other than energy and momentum conservation which limits the transmission. We find that the zero transmission originates from the different symmetries of the wavefunctions. In three-dimensional Brillouin zone, the lowest conduction band of sGe is at Γ point with $\Gamma_{2'}$ symmetry. Under the symmetry operation mentioned above $\hat{S} = \{C_4 | \tau_d\}$, it transforms as $\hat{S} |u_{R, \Gamma}\rangle = -|u_{R, \Gamma}\rangle$. In comparison, for the lowest conduction band of Si at Δ point, it satisfies $\hat{S} |u_{L, \Delta}\rangle = e^{ik_{L,z}a/4} |u_{L, \Delta}\rangle$. The Hamiltonian for a perfect Si/sGe interface should always have “even” symmetry Δ_1 . Hence, it follows that $\hat{S}\hat{H} = e^{ik_{L,z}a/4}\hat{H}$ and $\hat{S}\hat{G} = e^{-ik_{L,z}a/4}\hat{G}$. As a result, the transmission matrix element should satisfy the condition, $t_{ji} \propto \langle u_{R, \Gamma} | \hat{G} | u_{L, \Delta} \rangle = \langle \hat{S}u_{R, \Gamma} | \hat{S}\hat{G} | \hat{S}u_{L, \Delta} \rangle = -\langle u_{R, \Gamma} | \hat{G} | u_{L, \Delta} \rangle$. Consequently, we obtain that $T_{ji} = |t_{ji}|^2 = 0$. Similarly, for the electrons at Δ point with $\mathbf{k} = (0, 0, k_{R,z})$, they have $\Delta_{2'}$ symmetry and transform as $\hat{S} |u_{R, \Delta}\rangle = -e^{ik_{R,z}a/4} |u_{R, \Delta}\rangle$. And we have $t_{ji} \propto \langle u_{R, \Delta} | \hat{G} | u_{L, \Delta} \rangle = \langle \hat{S}u_{R, \Delta} | \hat{S}\hat{G} | \hat{S}u_{L, \Delta} \rangle = -\langle u_{R, \Delta} | \hat{G} | u_{L, \Delta} \rangle$ hence $T_{ji} = 0$. In short, the transmission at $\bar{\Gamma}$ is exactly zero, dictated by symmetry.

V. TRANSMISSION THROUGH ROUGH INTERFACES

We add interface disorders in the form of atomic mixing. In particular, we randomly swap pairs of Si and Ge atoms that have the same distance to the interface. We use a larger supercell with in-plane periodicity to describe the rough interface. To mimic an actual rough Si/Ge interface observed in experiments[22], we make sure that the further away from the interface, the fewer or equal number of atom pairs are swapped. In the following, we define two measures of the degree of interface disorders along the interface normal and in the transverse directions.

The first measure is the number of atom layers that are involved in atomic mixing. If there are 2 layers of Si and 2 layers of Ge atoms are involved in atomic intermixing, the number of atoms that are swapped per layer follows a pattern of 1|2|2|1. We label such interface structure by 4 ml, in short for four mixing layers. A larger ml number corresponds to the larger degree of disorders in the cross-plane direction. The atomic number density of Si across the rough interface with different mixing layers can be found in Fig. A1 in the Appendix.

The second measure is the size of the transverse supercell. For example, when we construct a 2×2 transverse supercell with 4 ml structure, there are 2 out of 4 atoms for the Si atom layer closest to the interface and 1 out of 4 atoms

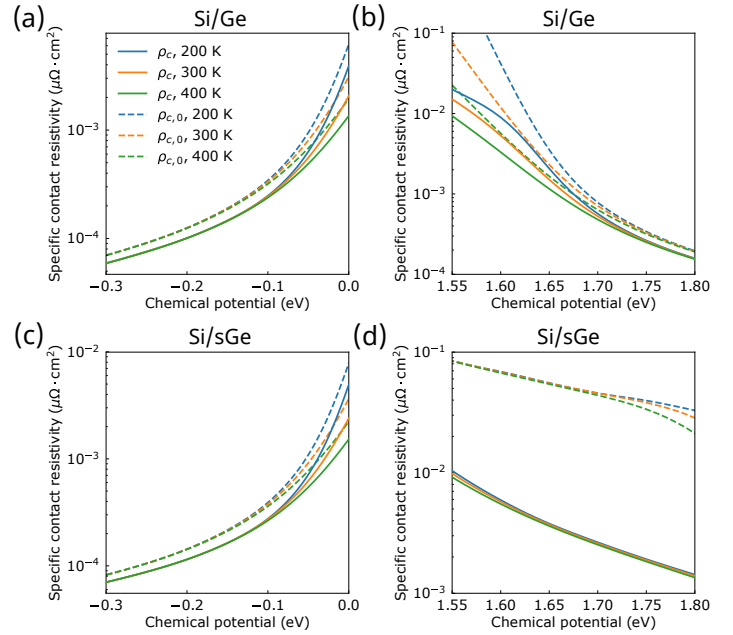


Figure 5. The specific contact resistance for (a) electrons and (b) holes for rough Si/Ge interfaces in solid lines and for the perfect Si/Ge interface in dashed lines at various temperatures. The specific contact resistance for (c) electrons and (d) holes for rough Si/sGe interfaces in solid lines and the perfect Si/sGe interface in dashed lines at various temperatures.

for the Si atom layer secondly closest to the interface involved in atomic mixing. When we use a larger transverse supercell (3×3 or 4×4), we let the number of swapped atoms unchanged. Effectively, the larger transverse supercell we use, the smaller degree of disorders along the transverse directions. For a given ml number and a given supercell size, we generate 21 random configurations and compute the ensemble average of the transmission and reflection probability matrix elements.

We found that the total transmissions for electrons and holes are both enhanced for rough Si/Ge and Si/sGe interfaces compared with the corresponding perfect interfaces, as shown in Fig. 4 (a)-(d). Particularly, for the Si/sGe interface with energy E ranging from 1.5 eV to 1.9 eV, almost all transmission channels are nonspecular, while it is zero for the perfect interface. For the hole transmission, we notice that the nonspecular part is much smaller than the specular part and the enhancement in the total transmission is not significant, although the transmission for both electrons and holes are enhanced by the rough interface compared with the perfect interface. This is because holes are close to $\mathbf{k} = 0$ and have long wavelengths. In Appendix Fig. A2, we have shown the dependence of transmission function on the degree of disorders along transverse and longitudinal directions. It turns out that the smaller transverse supercell dimensions and large mixing layer numbers are in favor of the nonspecular transmission. The smaller transverse supercell provides a large \mathbf{G}_{\parallel} , which allows the transition between the valleys far away in the reciprocal spaces. The larger degree of disorders along the perpendicular direction can fully

lower the lateral symmetry and provides channels that are previously forbidden by symmetry.

In Fig. 4 (e), we plot the mode-resolved specular transmission and reflection probabilities at $E = 1.77$ eV as a function of their unfolded momentum $\mathbf{k}_{\text{uc},\parallel}$. We find that the overlapped valleys for Si and sGe at $\bar{\Gamma}$ point now lead to small specular transmission probability. This is because the atomic mixing at the interface breaks the symmetry of Hamiltonian \hat{H} and the above-mentioned symmetry-forbidden transmission at $\bar{\Gamma}$ point is now allowed. In Fig. 4 (f), we show the nonspecular transmission and reflection probabilities. The majority of nonspecular transmission processes are found to be starting from the $\bar{\Gamma}$ and \bar{M} point in Si to the \bar{X} and \bar{Y} point in sGe. These processes correspond to the transition between the lowest conduction band of Si at Δ point and the lowest conduction band of Ge at L in the three-dimensional Brillouin zone. Recall that smaller transverse supercell dimensions are desired for high nonspecular transmission. This is because the Si's conduction band at Δ point and Ge's conduction band at L point are both far from Γ point and the electrons have small wavelengths. The characteristic length of disorders has to be small to contribute to the nonspecular interface scattering. In another word, we want to make the disordered structures ordered in a way that is favor of certain nonspecular transmission channels.

We can define the specular and nonspecular reflection probabilities similarly to the transmission. By examining the specular and nonspecular reflection probabilities, we find that the newly emerged nonspecular reflection channels are accompanied by the removal of the specular transmission channels at the same $\mathbf{k}_{\text{uc},\parallel}$. Although the increasing nonspecular reflection probability is detrimental for interfacial transport, there are overall more nonspecular transmission channels than the nonspecular reflection channels thus total transmission is still enhanced.

With the knowledge of the transmission function, we proceed to compute the contact resistance. The Landauer-Büttiker formalism is used to compute the two-probe conductance,

$$G_{12} = -\frac{2e^2}{h} \int dE \Theta(E) \frac{\partial f}{\partial E} \quad (10)$$

where h is the Plank constant, $f = \frac{1}{e^{(E-\mu)/k_B T} + 1}$ is the Fermi-Dirac distribution function and the factor 2 describes the spin degree of freedom. The subscripts 1 and 2 refer to the left and right sides. The four-probe conductance can be computed by[51, 59],

$$G_4 = \frac{1}{G_{12}^{-1} - \frac{1}{2} (G_{11}^{-1} + G_{22}^{-1})} \quad (11)$$

where G_{11} and G_{22} are the two-probe conductance for bulk material 1 and 2, respectively. In practical calculations of the conductance for a bulk material, we let the two leads and devices all consist of same materials. Then, the specific contact resistance is defined by,

$$\rho_c = \frac{A}{G_4} \quad (12)$$

where A is the cross-section area.

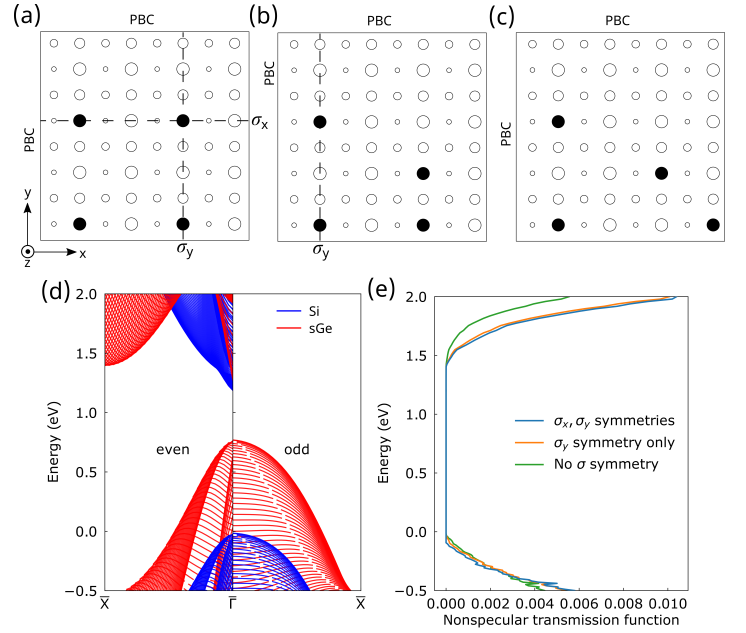


Figure 6. (a) The disordered structure with both σ_x and σ_y symmetry. (b) The disordered structure without σ_x yet with σ_y symmetry. (c) The disordered structure without σ_x and σ_y symmetry. σ_x and σ_y refer to the mirror symmetries along the x and y directions. In (a)-(c), the open circles are the Si atoms and the filled circles refer to the swapped Ge atoms. The larger circles represent the atoms closer to the interface. We only plot the Si side here, and on the Ge side the swapped Si atoms have the same transverse positions with the swapped Ge atoms on the Si side. (a)-(c) all correspond to 4×4 , 2 ml structures. (d) The projected bulk band structures of Si and sGe along $\bar{\Gamma}\bar{X}$ in the surface Brillouin zone sorted by their symmetries. (e) The nonspecular transmission function $\Theta_{\text{ns}}(E)$ for the three disordered interface structures plotted in (a)-(c).

In Fig. 5, we observe over an order of magnitude reduction of the contact resistance for Si/sGe interface at various temperatures compared with the perfect interface. For the rough Si/Ge interface, a much smaller reduction in resistance is found, because of the enhanced transmission for low energy conduction bands. For valence bands, the hole contact resistance for both interfaces is only slightly reduced by the interface disorders.

Last but not least, we want to examine how the symmetry of the disordered interface changes the nonspecular transmission. The nonspecular transmission probability can be analyzed using perturbation theory[42, 60] and we argue that the nonspecular transmission probability is proportional to the scattering matrix element, $t_{ns,ji} \propto \langle u_j | \Delta H | u_i \rangle$, where the perturbed potential is the difference between the potential energy for disordered interface and perfect interface, $\Delta H = H_{\text{rough}} - H_{\text{perfect}}$. For different disordered interface structure, the symmetry of ΔH can be different.

In Fig. 6, we show the nonspecular transmission for three representative disordered interface configurations. In Fig. 6 (d), we have plotted the projected band structures of Si and sGe, sorted according to the symmetries of Bloch wavefunctions under mirror operation. The conduction band for Si

It has been pointed by Khomyakov *et al.*[41] that the eigenvalue $\Lambda_{R,i}^r$ stores the phase information of the electron and the eigenvector matrix $U_{R,i}^r$ contains the Bloch wavefunctions for state i . If $|\Lambda_{R,i}^r| \neq 1$, it corresponds to an evanescent state. If $|\Lambda_{R,i}^r| = 1$, it corresponds to a propagating state. We can extract the perpendicular momentum by $k_{R,i} = \frac{1}{a_R} \log \Lambda_{R,i}^r$. Similarly, for the left lead, we define the auxiliary matrix, its eigenvalues and eigenvectors,

$$\begin{aligned} F_L^a &= g_L^a H_{01}^L \\ F_L^a U_L^a &= \Lambda_L^a U_L^a \end{aligned} \quad (\text{A7})$$

where $g_L^a = (g_L^r)^\dagger$ is the advanced surface Green's function for the left lead.

The velocity along the transport direction (perpendicular to interface) v_z can be described by the velocity matrix,

$$\begin{aligned} V_L^a &= -U_L^{a\dagger} \Gamma_L^a U_L^a, \\ V_R^r &= U_R^{r\dagger} \Gamma_R^r U_R^r. \end{aligned} \quad (\text{A8})$$

where $\Gamma = i(\Sigma - \Sigma^\dagger)$. The diagonal elements of these matrices correspond to the group velocities along z direction of different states.

The reflection probability matrix from α side $R_{\alpha\alpha,ji}(E, \mathbf{k}_{\text{sc},\parallel})$ is similarly defined by,

$$R_{\alpha\alpha,ji}(E, \mathbf{k}_{\text{sc},\parallel}) = |r_{\alpha\alpha,ji}(E, \mathbf{k}_{\text{sc},\parallel})|^2 \quad (\text{A9})$$

Specifically, the reflection matrices from the left and right side are,

$$\begin{aligned} r_{LL}(E, \mathbf{k}_{\text{sc},\parallel}) &= i\sqrt{V_L^r} [U_L^r]^{-1} (G_{0,0} - Q_L^{-1}) [U_L^{a\dagger}]^{-1} \sqrt{V_L^a} \\ r_{RR}(E, \mathbf{k}_{\text{sc},\parallel}) &= i\sqrt{V_R^r} [U_R^r]^{-1} (G_{N+1,N+1} - Q_R^{-1}) [U_R^{a\dagger}]^{-1} \sqrt{V_R^a} \end{aligned} \quad (\text{A10})$$

where $Q_L^{-1} = (E + i\eta)I - H_{00}^L - H_{10}^L g_L^r H_{01}^L - H_{01}^L g_L^r H_{10}^L$ and $Q_R^{-1} = (E + i\eta)I - H_{00}^R - H_{01}^R g_R^r H_{10}^R - H_{10}^R g_R^r H_{01}^R$ are the retarded Green's functions for bulk materials. $g_{\alpha'}^r$, $\alpha = L, R$ are the retarded surface Green's function similar to Eq. A4, except that they describe the semi-infinite lead of the same material extending to infinity in the opposite direction, and they are given by,

$$\begin{aligned} g_{L'}^r(E, \mathbf{k}_{\text{sc},\parallel}) &= [(E + i\eta)I - H_{00}^L - \Sigma_{L'}^r]^{-1} \\ g_{R'}^r(E, \mathbf{k}_{\text{sc},\parallel}) &= [(E + i\eta)I - H_{00}^R - \Sigma_{R'}^r]^{-1} \end{aligned} \quad (\text{A11})$$

where the self-energies write,

$$\begin{aligned} \Sigma_{L'}^r &= H_{01}^L g_L^r H_{10}^L \\ \Sigma_{R'}^r &= H_{10}^R g_R^r H_{01}^R \end{aligned} \quad (\text{A12})$$

The reflection matrix also depends on another two surface Green's function g_L^r and g_R^a , as defined by Eq. A4. The auxiliary matrices, eigenvalue matrices and eigenvector matrices for these two surface Green's functions are,

$$\begin{aligned} F_L^r &= g_L^r H_{01}^L \\ F_L^r U_L^r &= \Lambda_L^r U_L^r \end{aligned} \quad (\text{A13})$$

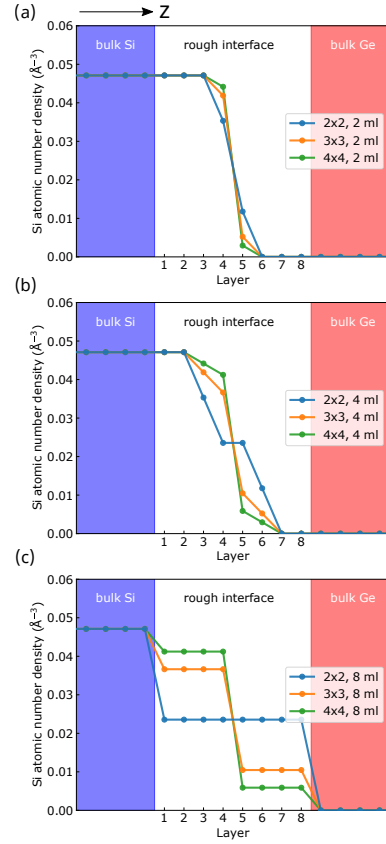


Figure A1. The atomic number density (the number of atoms of a given type per unit volume) of Si at different atom layers of the interface.

$$\begin{aligned} F_R^a &= g_R^a H_{10}^R \\ F_R^a U_R^a &= \Lambda_R^a U_R^a \end{aligned} \quad (\text{A14})$$

The self-energies for these two surface Green's functions are,

$$\begin{aligned} \Sigma_R^a &= H_{01}^R g_R^r H_{10}^R \\ \Sigma_L^r &= H_{10}^L g_L^a H_{01}^L \end{aligned} \quad (\text{A15})$$

The corresponding broadening matrices are computed by $\Gamma = i(\Sigma - \Sigma^\dagger)$. The velocity matrices V_R^a and V_L^r introduced in Eq. A10 are expressed by,

$$\begin{aligned} V_R^a &= -U_R^{a\dagger} \Gamma_R^a U_R^a, \\ V_L^r &= U_L^{r\dagger} \Gamma_L^r U_L^r. \end{aligned} \quad (\text{A16})$$

Appendix B: Interface atomic mixing

In Fig. A1, we present the ensemble-averaged atomic number density along z direction for different ml and transverse supercell sizes. In Fig. A2, we demonstrate the corresponding electron transmission for different interface configurations. At fixed ml number, smaller transverse supercell sizes give rise to higher nonspecular transmission function. At fixed transverse supercell size, the higher ml numbers give rise to higher nonspecular transmission function.

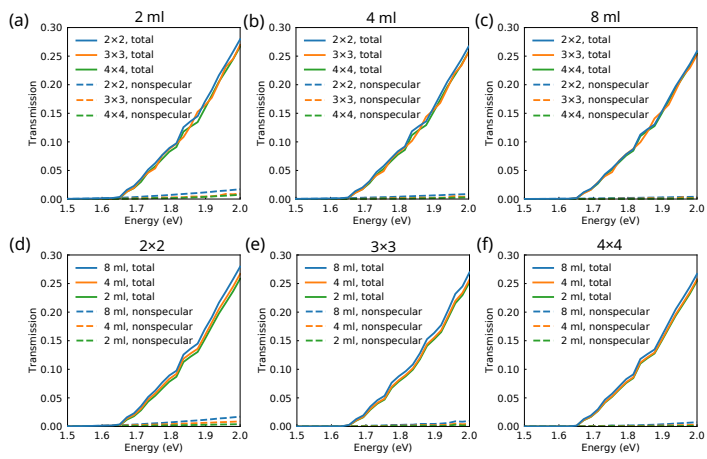


Figure A2. The sensitivity of electron transmission on the degree of transverse and longitudinal disorders. We use 20×20 , 15×15 , 10×10 $\mathbf{k}_{\text{sc},\parallel}$ -point mesh for 2×2 , 3×3 , 4×4 transverse supercells.

-
- [1] H. Kroemer, *Rev. Mod. Phys.* **73**, 783 (2001).
- [2] H. Soda, K.-i. Iga, C. Kitahara, and Y. Suematsu, *Japanese Journal of Applied Physics* **18**, 2329 (1979).
- [3] K. Tai, L. Yang, Y. Wang, J. Wynn, and A. Cho, *Applied Physics Letters* **56**, 2496 (1990).
- [4] M. Peters, B. Thibeault, D. Young, J. Scott, F. Peters, A. Gossard, and L. Coldren, *Applied Physics Letters* **63**, 3411 (1993).
- [5] H. Kroemer, *Proceedings of the IEEE* **70**, 13 (1982).
- [6] M. S. Lundstrom and R. J. Schuelke, *IEEE Transactions on Electron Devices* **30**, 1151 (1983).
- [7] H. Page, C. Becker, A. Robertson, G. Glastre, V. Ortiz, and C. Sirtori, *Applied Physics Letters* **78**, 3529 (2001).
- [8] B. Levine, C. Bethea, G. Hasnain, V. Shen, E. Pelve, R. Abbott, and S. Hsieh, *Applied Physics Letters* **56**, 851 (1990).
- [9] G. Chen, Taofang Zeng, *Microscale Thermophysical Engineering* **4**, 39 (2000).
- [10] G. Zeng, A. Shakouri, C. Bounty, G. Robinson, E. Croke, P. Abraham, X. Fan, H. Reese, and J. Bowers, *Electronics Letters* **35**, 2146 (1999).
- [11] S. Jain and W. Hayes, *Semiconductor Science and Technology* **6**, 547 (1991).
- [12] G. Scappucci, C. Kloeffel, F. A. Zwanenburg, D. Loss, M. Myronov, J.-J. Zhang, S. De Franceschi, G. Katsaros, and M. Veldhorst, *Nature Reviews Materials* , 1 (2020).
- [13] L. A. Terrazos, E. Marcellina, Z. Wang, S. N. Coppersmith, M. Friesen, A. R. Hamilton, X. Hu, B. Koiller, A. L. Saraiva, D. Culcer, and R. B. Capaz, *Phys. Rev. B* **103**, 125201 (2021).
- [14] N. F. Hinsche, I. Mertig, and P. Zahn, *Journal of Physics: Condensed Matter* **24**, 275501 (2012).
- [15] T. Koga, X. Sun, S. B. Cronin, and M. S. Dresselhaus, *Applied Physics Letters* **75**, 2438 (1999).
- [16] T. Koga, S. Cronin, M. Dresselhaus, J. Liu, and K. Wang, *Applied Physics Letters* **77**, 1490 (2000).
- [17] D. Vashaee and A. Shakouri, *Phys. Rev. Lett.* **92**, 106103 (2004).
- [18] R. Landauer, *IBM Journal of Research and Development* **1**, 223 (1957).
- [19] B. Laikhtman and S. Luryi, *Phys. Rev. B* **49**, 17177 (1994).
- [20] G. Chen, *Applied Physics Letters* **82**, 991 (2003).
- [21] D. Schroeder, *Modelling of Interface Carrier Transport for Device Simulation* (Springer Science & Business Media, 1994).
- [22] H. Takeuchi, P. Ranade, V. Subramanian, and T.-J. King, *Applied Physics Letters* **80**, 3706 (2002).
- [23] S. Datta, *Electronic Transport in Mesoscopic Systems* (Cambridge University Press, 1997).
- [24] A. Calzolari, N. Marzari, I. Souza, and M. Buongiorno Nardelli, *Phys. Rev. B* **69**, 035108 (2004).
- [25] N. Papior, N. Lorente, T. Frederiksen, A. García, and M. Brandbyge, *Computer Physics Communications* **212**, 8 (2017).
- [26] M. Paulsson and M. Brandbyge, *Phys. Rev. B* **76**, 115117 (2007).
- [27] J. Taylor, H. Guo, and J. Wang, *Phys. Rev. B* **63**, 245407 (2001).
- [28] S. Datta, *Superlattices and Microstructures* **28**, 253 (2000).
- [29] A. Rahman, J. Guo, S. Datta, and M. S. Lundstrom, *IEEE Transactions on Electron Devices* **50**, 1853 (2003).
- [30] O. V. Yazyev and S. G. Louie, *Nature Materials* **9**, 806 (2010).
- [31] D. Stradi, U. Martinez, A. Blom, M. Brandbyge, and K. Stokbro, *Phys. Rev. B* **93**, 155302 (2016).
- [32] B. Kretz, C. S. Pedersen, D. Stradi, M. Brandbyge, and A. Garcia-Lekue, *Phys. Rev. Applied* **10**, 024016 (2018).
- [33] G. E. W. Bauer, *Phys. Rev. Lett.* **69**, 1676 (1992).
- [34] J. Barnaś, A. Fuss, R. E. Camley, P. Grünberg, and W. Zinn, *Phys. Rev. B* **42**, 8110 (1990).
- [35] T. G. S. M. Rijks, R. Coehoorn, M. J. M. de Jong, and W. J. M. de Jonge, *Phys. Rev. B* **51**, 283 (1995).
- [36] J. Mathon, *Phys. Rev. B* **55**, 960 (1997).
- [37] E. Bellotti, F. Bertazzi, A. Tibaldi, J. Schuster, J. Bajaj, and M. Reed, *Phys. Rev. Applied* **16**, 054028 (2021).
- [38] A. Tibaldi, J. A. G. Montoya, M. G. C. Alasio, A. Gullino, A. Larsson, P. Debernardi, M. Goano, M. Vallone, G. Ghione, E. Bellotti, and F. Bertazzi, *Phys. Rev. Applied* **14**, 024037 (2020).
- [39] V. F. Los, *Phys. Rev. B* **72**, 115441 (2005).
- [40] V. Popescu and A. Zunger, *Phys. Rev. Lett.* **104**, 236403 (2010).
- [41] P. A. Khomyakov, G. Brocks, V. Karpan, M. Zwierzycki, and P. J. Kelly, *Phys. Rev. B* **72**, 035450 (2005).
- [42] Q. Song and G. Chen, *Phys. Rev. B* **104**, 085310 (2021).
- [43] G. Xia, J. L. Hoyt, and M. Canonico, *Journal of Applied Physics* **101**, 044901 (2007).
- [44] P. Hashemi and J. L. Hoyt, *IEEE electron device letters* **33**, 173 (2011).
- [45] B. Yang, W. Liu, J. Liu, K. Wang, and G. Chen, *Applied Physics Letters* **81**, 3588 (2002).
- [46] J.-M. Jancu, R. Scholz, F. Beltram, and F. Bassani, *Phys. Rev. B* **57**, 6493 (1998).
- [47] J. C. Slater and G. F. Koster, *Phys. Rev.* **94**, 1498 (1954).
- [48] Y. M. Niquet, D. Rideau, C. Tavernier, H. Jaouen, and X. Blase, *Phys. Rev. B* **79**, 245201 (2009).
- [49] We are interested in the interface scattering by the atomically rough interfaces. Hence, we focus on the domain within the range of \sim nm to the interface, where the lattice constant does not vary drastically. Thus, we assume the Si-Si, Ge-Ge bond lengths are the same with Si-Ge bond length of 2.3979 Å in the domain of our simulation. That is to say, the Si/Ge interface structure is the same with bulk Si's structure except some atoms are substituted by Ge atoms..
- [50] The band structure transits from Si to Ge with a discontinuity of valence band edge known as the valence band offset. In addition, depending on the carrier concentrations of Si and Ge side, the band structures of Si and Ge vary with distance to the interface known as band bending. The characteristic length of band bending is the Debye length, which is typically around \sim 10 to \sim 100 nm. Since we focus on the interface scattering in the proximity of rough interfaces (below 10 nm), we neglect the band bending and assume a constant band edge profile in Si side and Ge side. As for the band offset across the Si/Ge interface, we use the value of 0.68 eV for bond length $L = L_0 = 2.398$ Å..
- [51] D. S. Fisher and P. A. Lee, *Phys. Rev. B* **23**, 6851 (1981).
- [52] E. N. Economou, *Green's Functions in Quantum Physics*, Vol. 7 (Springer Science & Business Media, 2006).
- [53] V. Gurarie, *Phys. Rev. B* **83**, 085426 (2011).
- [54] M. S. Dresselhaus, G. Dresselhaus, and A. Jorio, *Group Theory: Application to the Physics of Condensed Matter* (Springer Science & Business Media, 2007).
- [55] L. P. Bouckaert, R. Smoluchowski, and E. Wigner, *Phys. Rev.* **50**, 58 (1936).

- [56] M. I. Aroyo, A. Kirov, C. Capillas, J. Perez-Mato, and H. Wondratschek, *Acta Crystallographica Section A: Foundations of Crystallography* **62**, 115 (2006).
- [57] J. Michel, J. Liu, and L. C. Kimerling, *Nature Photonics* **4**, 527 (2010).
- [58] H. Seo, R. C. Hatch, P. Ponath, M. Choi, A. B. Posadas, and A. A. Demkov, *Phys. Rev. B* **89**, 115318 (2014).
- [59] D. Ferry and S. M. Goodnick, *Transport in Nanostructures*, 6 (Cambridge University Press, 1999).
- [60] A. Brataas and G. E. W. Bauer, *Phys. Rev. B* **49**, 14684 (1994).
- [61] M. L. Sancho, J. L. Sancho, J. L. Sancho, and J. Rubio, *Journal of Physics F: Metal Physics* **15**, 851 (1985).
- [62] C. H. Lewenkopf and E. R. Mucciolo, *Journal of Computational Electronics* **12**, 203 (2013).
- [63] F. Sols, M. Macucci, U. Ravaioli, and K. Hess, *Journal of Applied Physics* **66**, 3892 (1989).